Available online at www.sciencedirect.com
SCIENCE DIRECT®
PERGAMON
International Journal of Multiphase Flow 29 (2003) 1203–1220
International Journal of Multiphase Flow
www.elsevier.com/locate/ijmulflow

A preliminary study of two-phase annular flow at microgravity: experimental data of film thickness

Pieter de Jong, Kamiel S. Gabriel *,1

Microgravity Research Group, University of Saskatchewan, 57 Campus Drive, Saskatoon, SK, Canada S7N 5A9

Received 10 June 2000; received in revised form 13 April 2003

Abstract

Film thickness time trace measurements were taken in normal (earth gravity) and microgravity (μ-g) conditions during parabolic flights operated by NASA Johnson Space Center in Houston, Texas. The measurements were taken using a parallel wire probe. Using the data, average film thickness, film minimum thickness, wave peak height, wave frequency and wave velocity were calculated over a wide range of liquid and gas mass velocities. The liquid mass velocity ranged from 49 to 318 kg/m^2 s, and the gas mass velocity ranged from 2.3 to 25 kg/m^2 s. While, based on average values of the film thickness, there were small differences between the 1-g and μ-g results, the wave base height and frequency were strongly affected by the reduction in gravity.
© 2003 Elsevier Ltd. All rights reserved.

Keywords: Annular flow; Two phase flow; Film structure; Microgravity flow; Film thickness measurements

1. Introduction

The phenomenon of two-phase flow in a near weightless environment (or microgravity) is becoming increasingly important. As power demands increase, two-phase flow loops are used in advanced spacecraft thermal management systems and also occur during the transfer of cryogenic propellants. On ground, two phase flow is common in power plants, transport of cryogenics, and many chemical and petrochemical processing plants. A simulated weightless environment allows for the investigation of parameters that are otherwise strongly masked by Earth's gravity. In the past, such studies allowed for the better predictions of the heat-transfer rates (Rite and Rezkallah,

* Corresponding author.
E-mail address: kamiel.gabriel@usask.ca (K.S. Gabriel).
[1] Formerly K.S. Rezkallah.

0301-9322/03/$ - see front matter © 2003 Elsevier Ltd. All rights reserved.
doi:10.1016/S0301-9322(03)00085-5

1994), and pressure drops (Zhao and Rezkallah, 1995), and flow regimes (Lowe and Rezkallah, 1998).

Annular flow is of particular interest because of its frequent occurrence in heat transfer systems. It is usually the preferred regime of operation for most heat transfer devices owing to the high heat-transfer rates associated with it. Although annular flow is dominated by the liquid and gas inertial effects, the detailed characteristics of the film structure could potentially be altered by the reduction in gravity. Such changes to the film structure are of significant interest in this study.

There are several studies on liquid film thickness measurements in annular gas–liquid flow at Earth gravity (which will be referred to hereafter as 1-g). For example, measurements were reported for vertical, upwards co-current flows of water–air mixtures by Willetts (1987), and Azzopardi (1986). At microgravity conditions, some measurements were taken and reported earlier by Bousman (1995). We will briefly discuss the main findings from these studies.

Willetts (1987) investigated the film thickness and wave properties in 1-g upwards flow. He took measurements in a 10.26 mm inside diameter tube using several gas–liquid mixtures including; air–water, air–aqueous sulpholane, air–genklene, air–fluoroheptane, and helium–water. By using these mixtures, Willetts was able to change the surface tension of the two-phase mixture. Under normal gravity conditions, body forces due to surface tension are masked by the overwhelming gravitational force and are usually discarded in two-phase flow models. Willetts reported very similar trends to the ones presented in this paper for 1-g conditions. He also proposed a correlation for the 1-g upwards flow film thickness that is not of direct use in microgravity flow.

Azzopardi (1986) focused his experiments on the characteristics of the disturbance waves in vertical, upwards annular two-phase flow. Measurements were taken using a water–air mixture in a 31.8 mm inside diameter tube. He reported trends in the film thickness that matched those of Willetts (1987). With careful analysis of the film thickness traces, he obtained and reported wave properties such as wave velocity, wave frequency and wave spacing.

Bousman (1995) measured the film thickness and other flow properties under microgravity conditions (parabolic flights). In his investigation of microgravity annular flow he used air–water, air–water/glycerin, and air–water/Zonyl FSP mixtures in a 12.7 mm inside diameter tube. In doing so, he attempted to examine the influence of changing the liquid viscosity and surface tension on the film thickness. He reported that an increase in the liquid viscosity led to a "thicker" film, while a reduction in the liquid–gas surface tension led to a "thinner" film. However, in his study, flow observations of the "thicker" or "thinner" film were made by the unassisted naked eye. Thus, it is difficult to conclude whether or not a "thick" film thickness may in fact be a film with larger disturbance waves that appears to the viewer as a "thick" film. On the other hand, Bousman's results observed similar trends in terms of film thickness reduction as the gas velocity increases.

2. The film thickness sensor

The method used to measure the film thickness is the parallel wire conductance technique. A pair of wires are stretched across the tube's cross section, and the electrical conductance between the two wires is measured. This conductance is indicative of the relative proportion of the phases in a particular cross sectional area. An individual probe consists of a pair of 40 μm stainless steel wires stretched across the pipe through 0.1 mm holes on opposite sides. A schematic of a cross

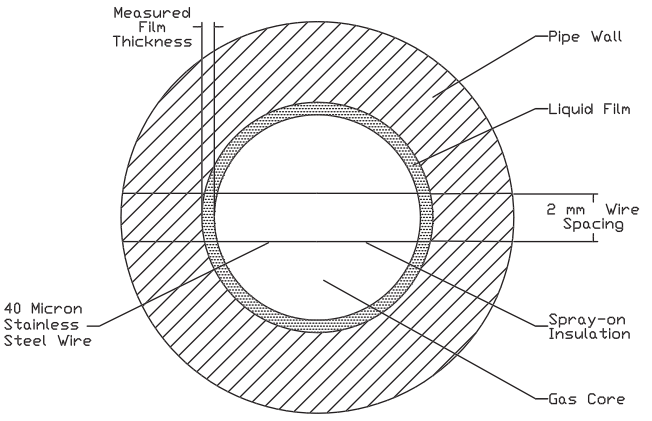

Fig. 1. A schematic of an individual film thickness probe.

section in a probe is shown in Fig. 1. Further details on the probe construction and electronics can be found in de Jong (1999).

There are three probes mounted on the flight apparatus. The first is a reference probe that is placed in the single-phase line. The second and third probes are mounted together at a distance equivalent to 110 tube diameters, D, (1.05 m) downstream of the mixer. The two probes are separated by a distance of $3D$ (28.6 mm).

3. Calibration and measurement accuracy

The film thickness sensor was calibrated using the following procedure. A syringe is used to inject a Taylor bubble into a gravity fed, constant head, downwards flow of water. The bubble rises until it encounters a vertical rod, which holds it in place across the film thickness sensor. The film thickness is varied by changing the amount of gas injected or the liquid flow rate. The film thickness is then measured using a micrometer needle probe. As the calibration varies with the conductivity of the fluid, it was therefore necessary to repeat the process after each flight. This resulted in two calibration curves (shown in Fig. 2), which are represented by the following two equations; one for each probe:

$$\delta_1 = 4.2302V^*, \quad \text{for probe 1, and} \tag{1}$$

$$\delta_2 = 4.0929V^*, \quad \text{for probe 2 (three tube diameters downstream of probe 1).} \tag{2}$$

In the above equations, V^* refers to a normalized value of the measured voltage ($V^* = (V_{\text{measured}} - V_{\text{allair}})/(V_{\text{allwater}} - V_{\text{allair}})$), δ is the measured value of film thickness in mm, subscript '1' refers to the downstream probe and the subscript '2' refers to the upstream probe. V_{allair} is the voltage the probe measures when the tube is completely filled with air, and V_{allwater} is the voltage the probe measures when the tube is completely filled with water. These voltages were measured during flight experiments. V_{measured} is the measured voltage. The second probe was used for cross-correlation to find the wave speed.

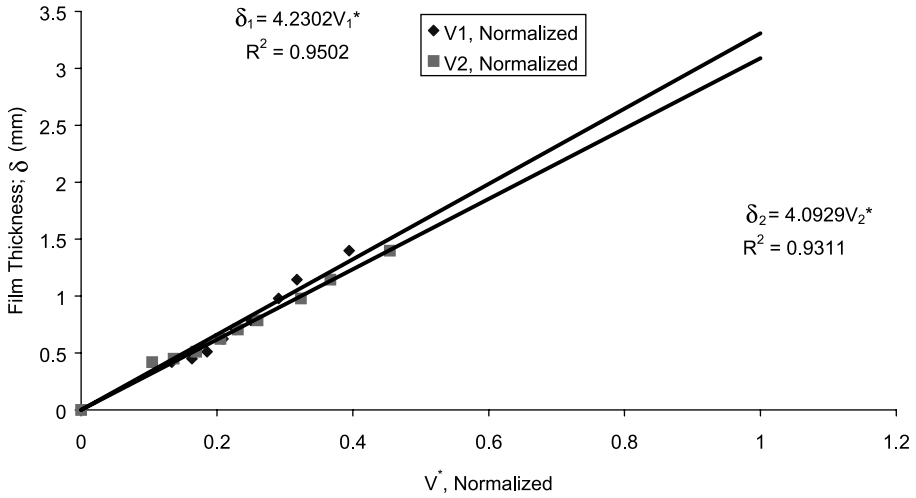

Fig. 2. Film thickness sensor calibration results, post-flight.

No method is presently known to the authors to measure the accuracy of the sensor in a dynamic situation. However the electronic components of each probe sample data at 1024 Hz. By examining the power spectral distribution results, it is clear that a sampling frequency of 500 Hz is sufficient to examine the frequencies associated with the film thickness time trace.

The uncertainty in the sensor measurements under static conditions can be estimated from two sources: (a) the bias uncertainty (uncertainty from calibration methods), and (b) the precision uncertainty (uncertainty due to system fluctuations). The bias uncertainty for this instrument is effectively the uncertainty of the micrometer which was used to calibrate the sensor (i.e. ±0.0254 mm). The precision uncertainty was estimated from the variability of the measured voltages at all air and all water conditions and was determined to be ±0.018 mm. This gives an estimated total uncertainty of ±0.045 mm.

4. Data source and experimental setup

A schematic of the experimental apparatus is shown in Fig. 3. A gear pump draws liquid from a "bladder" type tank and pumps it in a closed liquid loop. A turbine flow meter measures the volumetric flow rate of the liquid phase. A compressed air cylinder supplies the gas flow. The air flow rate is measured with a mass flow meter and a controller which delivers a preset flow of air into the mixer. Air is injected radially while the liquid passes axially through the mixing chamber. The 9.525 mm inside diameter test section begins at the outlet of the mixer. Gauge and absolute pressure measurements are taken 18.8 cm (~20*D*) downstream of the mixer. This is followed by a pair of viewing sections and a capacitance type void fraction sensor. The film thickness sensor has dual probes 30 mm (~3*D*) apart, located 1.05 m (~110*D*) downstream of the mixer. Finally the two-phase flow temperature and gauge pressure at the outlet of the test section are measured 1.24 m (~130*D*) downstream the mixer, which extends the differential pressure measurement over

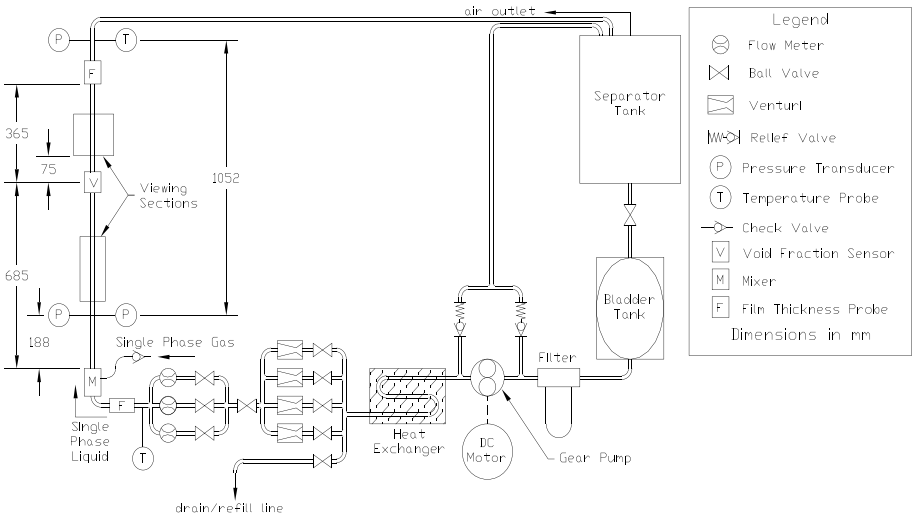

Fig. 3. A schematic of the two-phase flight apparatus.

1.052 m ($\sim$110D). The liquid portion of the flow is recycled using a separation tank. Complete separation takes place during the hypergravity portion ($\sim$1.8 g; on average) of the trajectory.

The microgravity experiments were conducted aboard the NASA DC-9, simulating a weightless environment by flying parabolic trajectories. During the ''free fall'' period, the equipment and personnel inside the cabin experience a near zero-gravity condition ($\pm$0.02 g; on average) for a period of up to 20 s. Measurements were also taken at earth's gravity (9.81 m/s^2) before and after each flight.

5. Data processing

Data collection starts prior to the microgravity period and terminates several seconds into the post-free-fall period. It is common that air turbulence would disturb the microgravity conditions causing vibrations and residual accelerations (known as g-jitter). This makes it necessary to select data ''windows'' in each parabola where such disturbances are a minimum. The selection of these ''windows'' is based on the measured gravity levels and the superficial gas and liquid velocities. The windows are selected such that the measured variables are within the following ranges: $g_{\text{level}} < \pm 0.02$ g, standard deviation of $V_{\text{sl}} < 7\%$, standard deviation of $V_{\text{sg}} < 2\%$; as used by Lowe (1997). Where g_{level} is the measured residual acceleration due to vibrations, V_{sl} is the superficial liquid velocity (m/s), and V_{sg} is the superficial gas velocity (m/s).

The data set used in this study contains set points in both annular and transitional flows (near the slug-to-annular region). Results are shown for both microgravity and earth gravity conditions. A sample of the film thickness time trace collected in microgravity is given in Fig. 4a. A corresponding flow sequence at earth gravity (vertical co-current upwards flow) is shown in Fig. 5a. Video images of the flow patterns associated with the film thickness traces in microgravity and

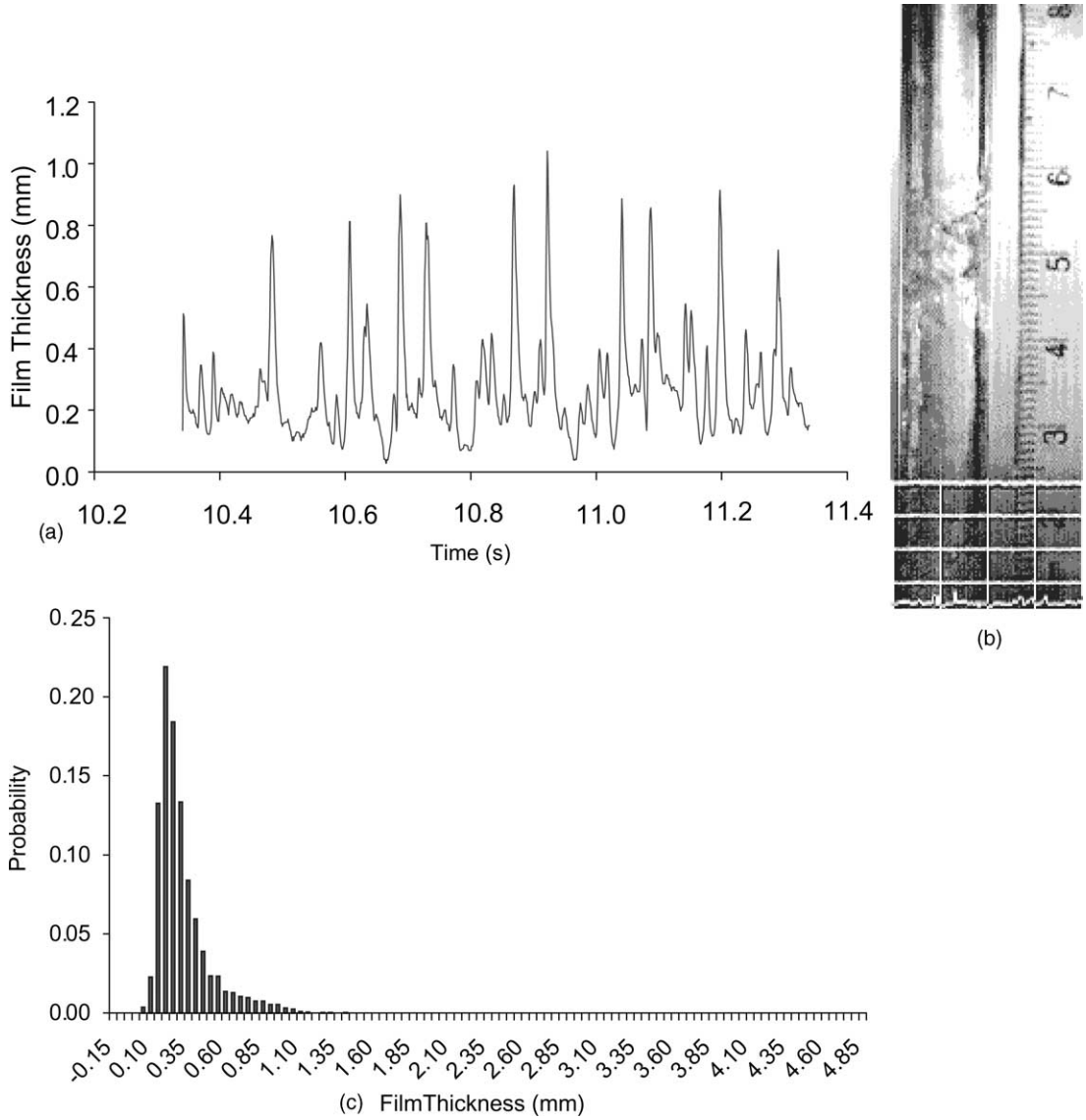

Fig. 4. (a) A sample of a film thickness time trace, Run 96F2P48 (microgravity). (b) Sample video image (microgravity) (96F2P48). (c) Sample PDF of film thickness trace (microgravity), (96F2P48).

earth gravity are shown in Figs. 4b and 5b, respectively. Probability distribution functions of the film thickness traces at μ-g and 1-g are shown in Figs. 4c and 5c, respectively.

Figs. 4 and 5 show parabolas P48 and P20, both of which have a gas mass flux of 25 kg/m^2 s and a liquid mass flux of 70.8 kg/m^2 s. Although it is not obvious to the unassisted eye when viewing the film thickness time trace, there are several differences between them. By analyzing the film thickness time traces, we can find that the waves on P48 are moving at 2.74 m/s as opposed to the

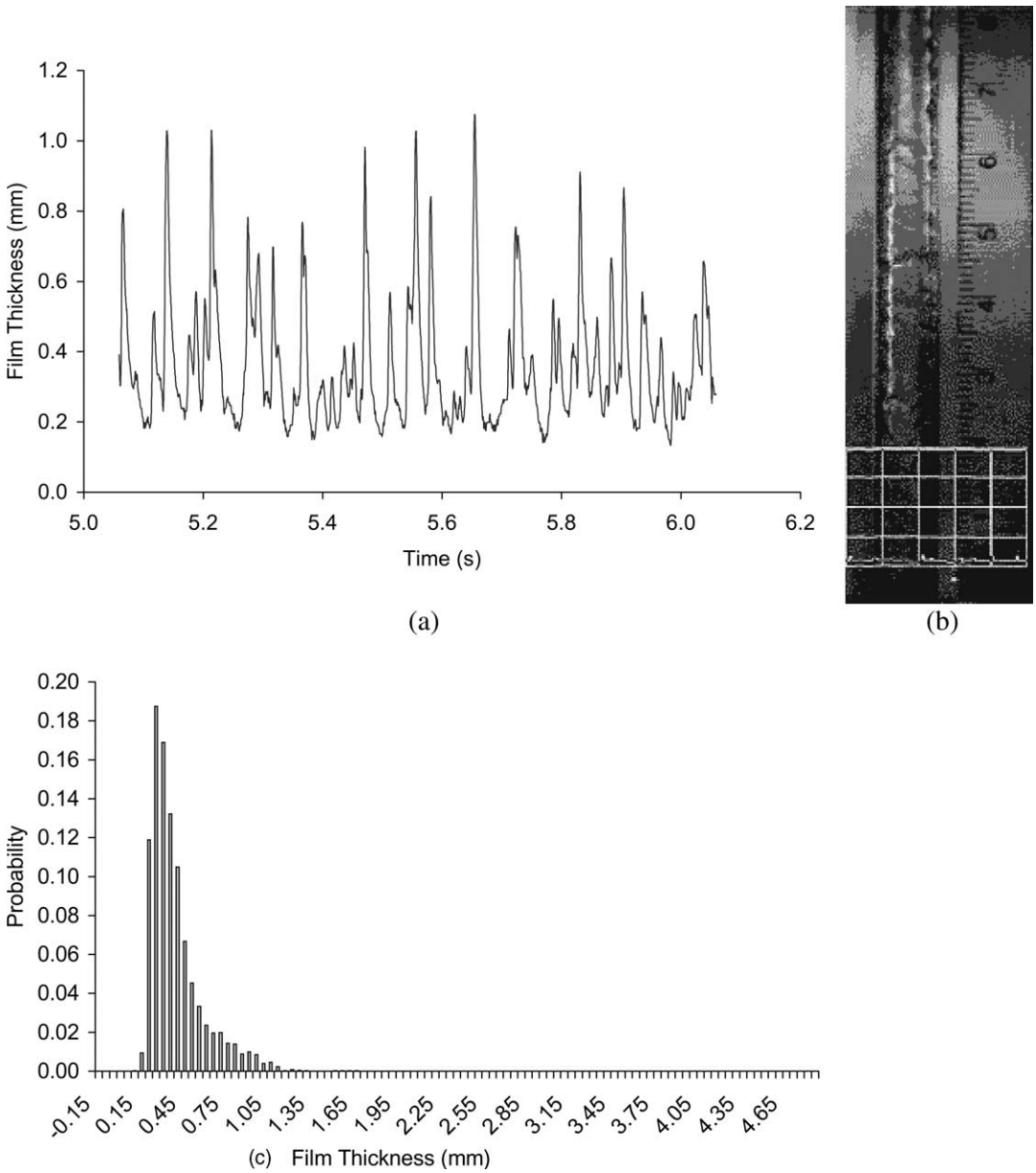

Fig. 5. (a) A sample of a film thickness time trace, run 96G3P20 (earth's gravity). (b) Sample video image (earth's gravity) (96G3P20). (c) Sample PDF of film thickness trace, (earth's gravity), (96G3P20).

wave on P20, moving at 2.66 m/s. As well, the average film thickness is 0.30 mm for P20 and 0.28 mm for P48. From the high speed video recordings, and to some extent in the still photographs of Figs. 4b and 5b, it can be clearly seen that the flow is still developing into the annular flow regime.

Data was collected at liquid mass fluxes ranging from 49 to 318 kg/m^2 s, and gas mass fluxes ranging from 2.3 to 25 kg/m^2 s. The original data included only the film thickness time traces.

A cursory examination of the two sample traces shows little differences between the two data sets. However, further analysis of the film thickness time traces show variations in terms of the average wave height, the substrate thickness, the average film thickness, the wave frequency, and the wave velocity. These parameters will be discussed separately in the following sections.

6. Film thickness results

The average film thickness is a time average value that is calculated over the length of the measurement window (0.3–1.0 mm seems typical). Fig. 6 shows the average measured film thickness plotted as a function of the gas mass flux. The data covers a wide range of liquid mass fluxes (49–318 kg/m^2 s), and includes both μ-g and 1-g data points.

As can be seen from the figure, changing the gas mass flux, G_g (kg/m^2 s), has a significant influence on the film thickness in that the latter decreases as G_g increases. The change is clearly not a linear process and hints at an asymptote as G_g increases to high mass fluxes. Increasing the liquid mass flow rate, on the other hand, has less effect on the film thickness. However it was observed that with increasing the liquid flow rate, the film thickness increases at a constant gas mass flux. Similar trends were observed in the 1-g data, primarily due to the fact that annular flow is dominated by the increasing effects of gas and liquid inertial forces compared to the forces due to gravity.

Examining the results shown in Fig. 6, it can be seen that for given gas and liquid mass flow rates, a reduction in the gravity force has a minimal effect on the film thickness. The average difference is in the order of 11% (being smaller for the microgravity case). This difference is not significant particularly when the measurement uncertainty is considered. It can also be seen that the difference in the film thickness is reduced as the gas mass flux increases. The difference at

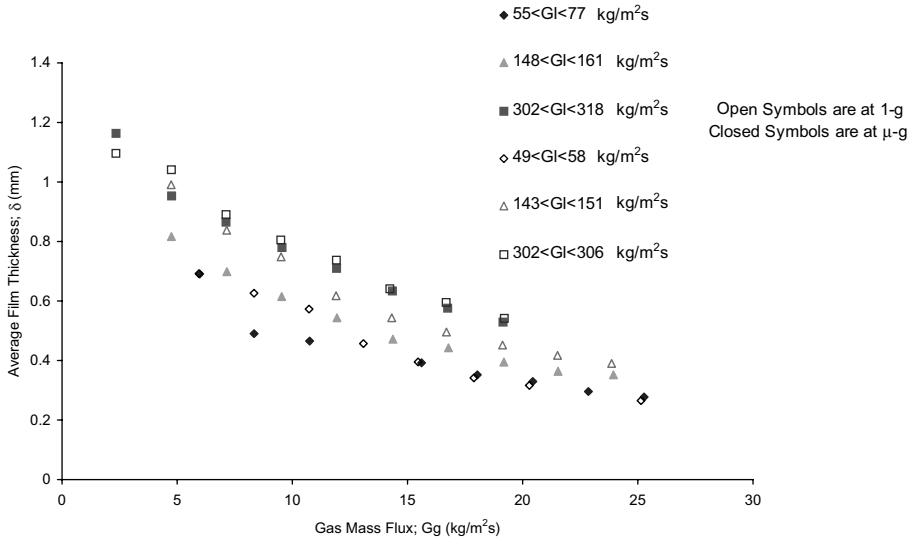

Fig. 6. Average film thickness as a function of gas mass flux, 1-g and μ-g data.

$G_g = 4.7$ kg/m^2 s, on average, is 15%, while at $G_g \approx 20$ kg/m^2 s, the average difference is only 6%. These changes are very small, but the trend is consistent in that the tendency is towards a "thinner" film at μ-g.

The observed trends can perhaps be explained using fundamental principles of fluid dynamics. Increasing the gas mass flux results in a higher gas velocity in the core, and hence a higher momentum transfer to the film. As a consequence, the average liquid velocity in the film increases. Therefore, for the same liquid film flow, assuming no significant entrainment, some reduction in the average film thickness is observed. On the other hand, as the liquid mass flux increases, more fluid is transported in the film. Since the fluid is incompressible, then the average liquid film velocity may increase or the thickness of the film may increase.

From the measured values of the average film thickness, it is clear that at least part of the effect of increasing the liquid mass flux "G_l" is to increase the thickness of the film. Examining the data for a gas mass flux fixed at 14.3 kg/m^2 s, it is seen that as the liquid mass flux is increased by about 85% (from 109.8 to 202.5 kg/m^2 s), the average film thickness increases by 26% (from 0.44 to 0.56 mm). This amounts to a net increase in the average film cross sectional area of about 25%. Since the fluid is incompressible and the cross sectional area has not increased in proportion to the increase in the liquid mass flux, it is therefore safe to conclude that the liquid film must have accelerated. Examination of the video records taken at high speed (1000 fps) seems to support this conclusion.

Another point to make here, which can also be inferred from Fig. 6, is that the difference between the 1-g and μ-g data significantly lessens as the mass fluxes of both phases increase. This is due to the fact that as the mass flux of both phases increases, the effect of gravitational forces (relative to inertial forces) is substantially reduced. On a unit volume basis, inertial effects are proportional to ρV^2, while gravitational effects are proportional to ρg. In the case of increasing the gas mass flux, the gas velocity increases. Since the liquid is accelerated by the fast moving gas flow, its velocity increases as well. Alternatively, as demonstrated by the numerical example above, increasing the liquid mass flux results in a faster moving film. Therefore, the inertia of the flow is increased relative to the gravitational force acting on the fluid in the opposite direction (case of vertical upwards flow). This tends to minimize the effects of gravitational forces on the flow as mass fluxes increase.

7. Wave properties

In annular flow, the surface of the film is not smooth. Instead, it is covered with dynamically active ripples generally referred to in the literature as "disturbance waves". In the following sections we will discuss the influence of changing the gas and liquid flow rates and gravity level on the disturbance wave properties. These properties include the wave frequency, wave velocity and wave magnitude and substrate height.

It should be noted here that although the ripples on the film are referred to in the literature as "disturbance waves", it is generally agreed that they do not actually correspond to liquid waves as seen on large bodies of water. Unlike actual waves, they demonstrate the ability to move liquid mass in the direction of the wave travel. In addition, they do not have a consistent and regular period to qualify as waves. Perhaps the most suitable description of these disturbances is that they

represent lumps of fluid rolling over a smooth substrate layer of the liquid film. As well there is a second set of disturbances to the surface of the film, referred to in the literature as "ripple" waves which are much smaller scale events that have not been heavily investigated. The classification and modeling of both types of "waves" is the subject of ongoing research at the Microgravity Research Group, University of Saskatchewan, Canada.

7.1. Wave velocity

The wave velocity was determined by cross correlating the two film thickness signals to find the best fit time lapse between them. A wave velocity was then calculated since the distance between the sensors is known. In Fig. 7, the wave velocity is plotted as a function of the gas mass flux for liquid mass fluxes ranging from 49 to 318 kg/m^2 s, at both μ-g and 1-g conditions. It is clearly seen that the wave velocity increases in an approximately linear fashion with increasing the gas mass flux. The same trend applies to both the 1-g and the μ-g data. The wave velocity is also seen to increase linearly with increasing the liquid mass flux. There is an indication of an asymptote occurring at the upper end of the gas mass fluxes examined. These observations are consistent with those reported by Azzopardi (1986) for vertical upwards co-current flow at 1-g.

For the 1-g case, at small gas and liquid mass fluxes, the wave velocity is sometimes a negative value. This is not surprising since in vertical upwards flow, a falling film occurs at low liquid mass fluxes due to the downward pull by gravity. If the "hold-up" of the liquid phase is small, body forces will cause the liquid film to drain and fall downwards.

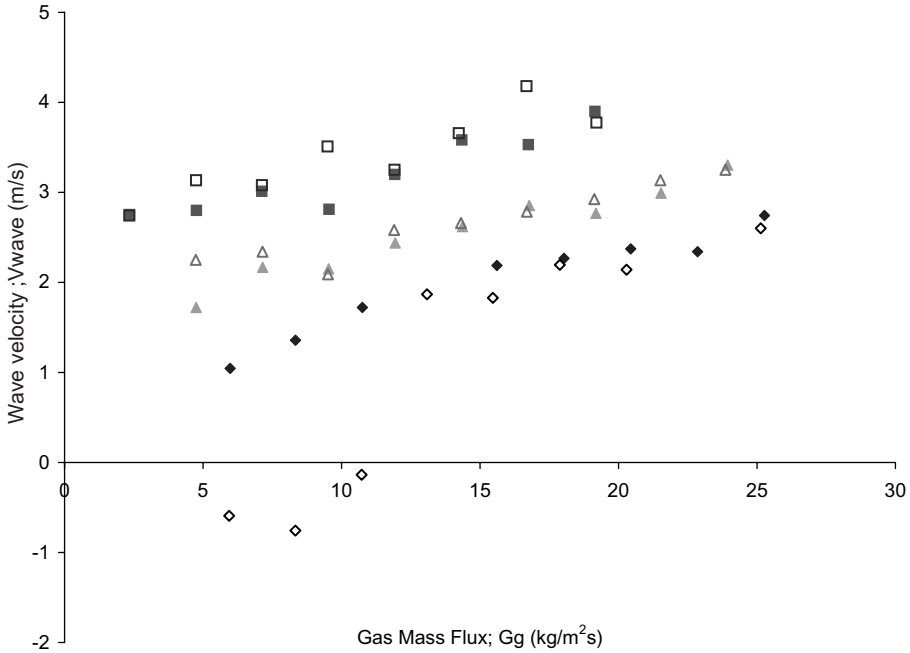

Fig. 7. Average wave velocity as a function of gas mass flux, 1-g and μ-g data.

It was shown earlier that at a gas mass flux of 14.3 kg/m^2 s, when the liquid mass flux increased by 85%, the average film thickness only increased from 0.44 to 0.56 mm. This represents approximately a 25% increase in the average film cross sectional area. Assuming that the entrained liquid fraction is zero, and taking the liquid density to be 998 kg/m^3, the difference in the average film velocities between these two cases amounts to about 0.58 m/s.

Using the same data points and the calculated wave velocities, at $G_l = 109.8$ kg/m^2 s, the wave velocity is estimated to be 2.22 m/s, and at $G_l = 202.5$ kg/m^2 s, the wave velocity is 2.74 m/s. The difference is 0.52 m/s, which is within 12% of the values previously calculated. Thus, it seems likely that the increase in the wave velocity with increasing the liquid mass flux could be attributed to the acceleration of the substrate over which the waves are traveling. Similar results were obtained when calculations were made for other fixed gas mass fluxes. However, at lower gas mass fluxes (approaching the slug-annular transition flow), the percentage difference becomes much larger ($\sim$60%). Repeating the procedure using the 1-g data set gives similar results except for the cases where falling film flow occurred.

Disregarding the points where a falling film due to gravity was observed, the RMS deviation between the 1-g and μ-g data is less than 10%. Unlike the substrate, the waves are not slowed down by the presence of gravity except for the situation when falling film occurs. Since the wave velocity is primarily driven by the velocity of the gas core, and since the latter is relatively unaffected by gravity forces (the gas density is much smaller than that of the liquid film), it is not surprising to obtain small differences in the wave velocity between the 1-g and μ-g cases.

7.2. Wave height and wave minimum

Quantitative measurements of the magnitude of the disturbance waves were calculated from the film thickness traces. A criterion was established to identify disturbance waves in the time trace. When a portion of the time trace had a height exceeding the critical value it was defined as a disturbance wave. The critical value, also referred to as the wave transition height, was determined from:

$$\delta_{\text{trans}} = \overline{\delta} + \sigma_\delta \tag{3}$$

where δ_{trans} is the wave transition height, $\overline{\delta}$ is the average value of the film thickness time trace, and σ_δ is the standard deviation of the film thickness time trace.

The wave height for an individual wave is of course the maximum value obtained in that particular section of film thickness time trace. These values were then averaged to obtain a wave height (H) for each parabola. The wave minimum height is representative of the scale of the liquid film beneath the disturbance waves. An individual wave minimum is simply the minimum film thickness measured in the film thickness time trace between a pair of disturbance waves. As with the wave heights, these values were then averaged for each parabola, obtaining the wave minimum height (h). In Figs. 8 and 9, the wave height and wave minimum are plotted as a function of the gas mass flux for both the 1-g and μ-g data sets.

From Fig. 8, it is seen that as the gas mass flux increases, the average wave peak height decreases in a way similar to that seen with the average film thickness. This trend is observed for both the μ-g and 1-g cases. Examining the wave minimum height data in Fig. 9, similar trends to

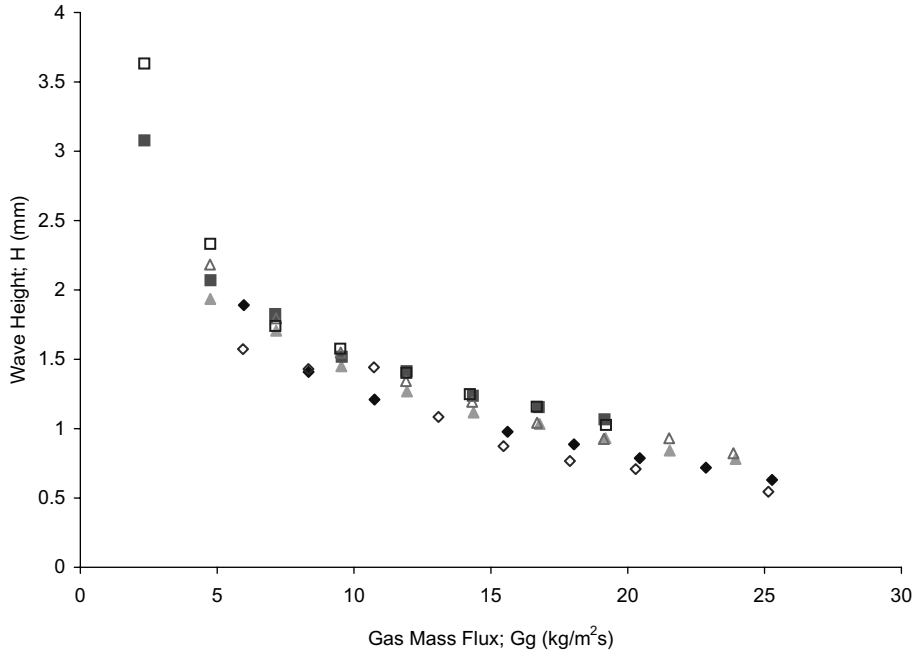

Fig. 8. Average wave height as a function of gas mass flux, 1-g and μ-g data.

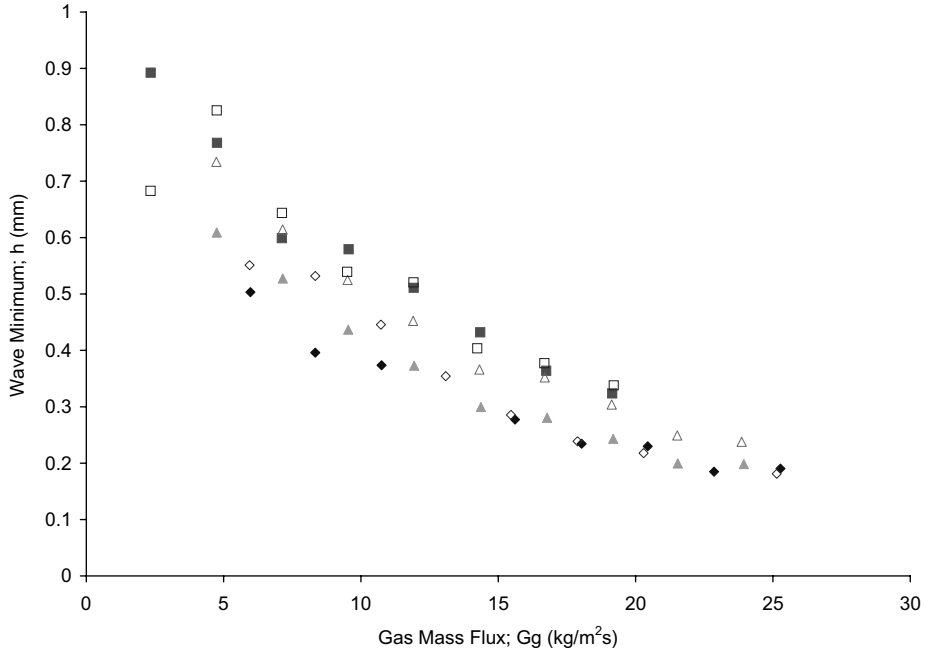

Fig. 9. Average wave minimum as a function of gas mass flux, 1-g and μ-g data.

the average film thickness are observed. A decrease in the wave minimum occurs with increasing the gas mass flux, and an increase of the wave minimum with increasing the liquid mass flux.

The presence of gravity has very little effect on the average wave height at high gas and liquid mass fluxes, with an average percent difference of less than 3.5% (the RMS deviation is less than 5%). However at low gas mass fluxes ($G_g \sim 5$ kg/m^2 s), the average percent reduction in wave height is 12.7%, whereas at high gas mass fluxes ($G_g \sim 20$ kg/m^2 s), the average change is only 1%. A similar effect is observed when varying the liquid mass flux. At low liquid mass fluxes ($G_l \sim 100$ kg/m^2 s), the average percent reduction is 5%, while at high liquid mass fluxes ($G_l \sim 300$ kg/m^2 s), the average reduction is 1.2%.

In comparison, the substrate height is significantly different between the 1-g and μ-g cases, being consistently thicker for the 1-g case. The average RMS percent difference in the substrate height is 12%.

Similar to previous cases, the substrate height shows a higher average percent difference at low liquid mass fluxes than at higher liquid mass fluxes (17.2% at $G_l \sim 100$ kg/m^2 s, compared to 1.6% at $G_l \sim 300$ kg/m^2 s). Again, this reduction in percent difference shows that the influence of gravity on annular flow decreases as inertial effects become more significant than those due to gravity.

The different percentages given for reduction in wave height and wave minima have implications with regards to how the wave substructure changes in the presence of gravity. Using the wave height less the wave minimum $(H - h)$ as an estimate of the overall scale of the wave, the data of Figs. 8 and 9 are used in Fig. 10. It is apparent that the scale of the wave is not affected by gravity level. The reduction in the average film thickness appears to be due to the "thinning" of the substrate layer.

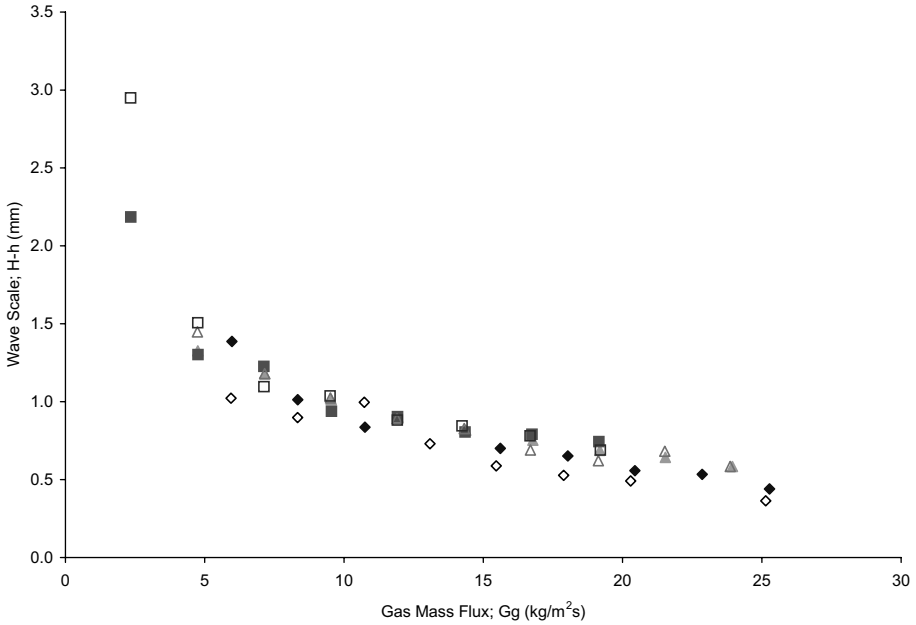

Fig. 10. Average wave scale $(H - h)$ as a function of gas mass flux, 1-g and μ-g data.

This perhaps could explain the visual observations reported by some researchers for the μ-g case. In those tests (Bousman, 1995), the film on the wall was described as a "thick" film due to the high activity in the film observed by naked eye. The present authors suggest that such observations could be perhaps explained in that the larger relative wave amplitude (wave scale has not decreased, while the substrate has thinned out) overlaying the substrate surface give the appearance of a "thicker" film.

7.3. Wave frequency

In this study, the wave frequency, ω_{wave}, was calculated by counting the number of occurrences when the wave transition height was exceeded and dividing it by the duration of time over which this occurred. In Fig. 11, the average frequency of the disturbance waves is plotted as a function of the gas mass flux for both 1-g and μ-g data.

Several interesting observations can be made from the results shown in Fig. 11. It is clear that the average wave frequency increases with increasing the gas mass flux. For both the μ-g data and 1-g data, there are indications that asymptotic values are being approached at gas mass fluxes of greater than 20 kg/m^2 s. The average wave frequency also increases with increasing the liquid mass flux. These trends are very similar to those reported by Azzopardi (1986) for ground based vertical upwards co-current flow in circular tubes.

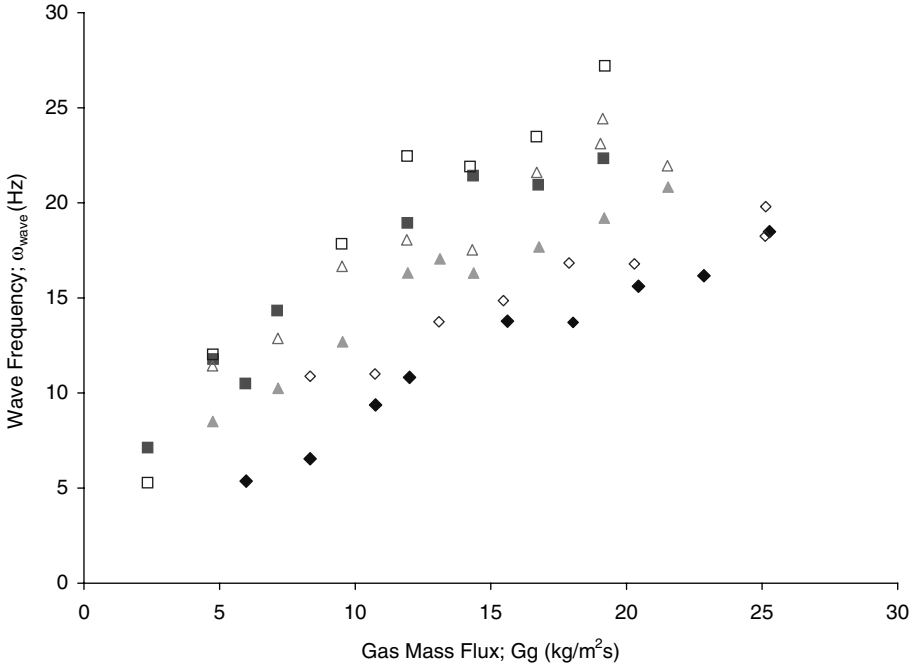

Fig. 11. Average wave frequency as a function of gas mass flux, 1-g and μ-g data.

A numerical examination of the data yields that at comparable data points, the wave frequency is on average 18% higher in μ-g conditions. Again, this difference is reduced when G_g is increased from an average of 40% at $G_g \sim 7.1$ kg/m^2 s, to 15% at $G_g \sim 20$ kg/m^2 s.

8. Conclusions

An experimental study of the film characteristics in annular flow was carried out at a simulated microgravity condition experienced onboard NASA's DC-9 zero gravity aircraft. Film thickness measurements were taken during flight tests along with high speed video imaging, pressure drop and void fraction data. The film properties were obtained from the film thickness time traces. The results can be summarized as follows.

(1) Accurate film thickness time traces were collected in annular and slug-annular transitional flow regimes over a range of gas mass fluxes from 2.3 to 25 kg/m^2 s, and for liquid mass fluxes ranging from 49 to 318 kg/m^2 s.
(2) From the film thickness traces, the average wave minimum height, the average film thickness, and the average wave height were calculated. The velocity and average frequency of the disturbance waves were also calculated using statistical techniques.
(3) At a fixed liquid mass flux it was shown that increasing the gas mass flux results in a thinner film, a higher wave velocity, and a higher wave frequency. On the other hand, increasing the liquid mass flux at a constant gas mass flux results in a thicker film, an increase in the wave velocity due to the acceleration of the liquid in the film, and a slight increase in the wave frequency.
(4) The wave velocity is mostly unaffected by the reduction in gravity except in regions of falling film flow at 1-g vertical flow. The wave frequency decreases with the reduction in gravity. There is some hint that the disturbance waves on the film are unaffected by a transition to a microgravity environment. Additional studies and data gathering in microgravity are needed to further examine this behaviour.

Acknowledgements

This project was co-sponsored by the Natural Science and Engineering Research Council of Canada (NSERC), and the Canadian Space Agency. We acknowledge the superb support that was received during the NASA DC-9 flight campaign.

Appendix A. Film thickness data

This appendix tabulates the film thickness data presented in this work. The data is presented in Tables 1 and 2, one for the data collected in a microgravity environment, and the other for 1-g upwards flow. Each set point is represented by a code such as 96F2P20. This code gives the year the data was collected, (1996), whether the data was collected during microgravity flights (F) or at

Table 1
Microgravity data, film thickness data

Code	δ (mm)	h (mm)	H (mm)	V_{Wave} (m/s)	ω_{wave} (Hz)	G_g (kg/m^2 s)	G_l (kg/m^2 s)	G_{level} (g)	Pabs (kPa)
96F2P2	0.496	0.279	0.897	1.75	10.12	4.750365	156.6391	0.0009	89.00
96F2P3	0.442	0.281	0.796	2.2	10.69	7.155548	155.6449	0.0059	89.00
96F2P4	0.404	0.229	0.706	2.18	13.58	9.536327	160.6336	0.0018	89.04
96F2P5	0.357	0.208	0.646	2.47	15.68	11.93753	156.6427	−0.0003	89.05
96F2P6	0.323	0.195	0.566	2.66	17.86	14.36633	155.6485	0.0007	89.07
96F2P7	0.308	0.177	0.52	2.9	20.52	16.77914	152.6553	0.0007	89.07
96F2P8	0.283	0.191	0.48	2.81	20.24	19.18392	150.6633	0.0013	89.11
96F2P10	0.279	0.198	0.47	3.04	20.73	21.53498	150.6667	0.0020	89.20
96F2P11	0.259	0.176	0.428	3.35	22.43	23.94053	148.6746	−0.0007	89.22
96F2P12	0.367	0.217	0.603	2.78	21.85	14.36513	202.5426	−0.0006	89.26
96F2P13	0.345	0.226	0.577	2.83	21.56	16.77271	204.5429	0.0001	89.24
96F2P14	0.318	0.21	0.531	3.18	21.02	19.16349	202.5473	−0.0009	89.26
96F2P15	0.577	0.324	1.026	2.33	10	3.556753	220.497	0.0004	89.24
96F2P16	0.537	0.31	0.907	2.12	13.57	5.952726	221.4998	−0.0006	89.27
96F2P18	0.459	0.272	0.786	2.08	15.75	8.320244	200.5518	−0.0004	89.29
96F2P19	0.418	0.253	0.732	2.39	16.39	10.73025	197.5585	−0.0009	89.32
96F2P20	0.383	0.239	0.66	2.63	18.4	13.1278	195.5674	0.0005	89.40
96F2P21	0.697	0.319	1.57	2.79	7.35	2.344322	308.3038	0.0008	89.39
96F2P22	0.589	0.358	1.04	2.84	12.39	4.757516	308.3109	−0.0009	89.48
96F2P23	0.544	0.308	0.91	3.06	16.96	7.119446	306.3154	0.0000	89.58
96F2P24	0.494	0.309	0.794	2.86	19.7	9.54989	302.3243	−0.0017	89.45
96F2P26	0.456	0.292	0.726	3.25	19.87	11.92059	317.2982	0.0003	89.58
96F2P27	0.419	0.273	0.666	3.64	21.43	14.34219	312.3164	−0.0014	89.66
96F2P28	0.387	0.255	0.601	3.58	24.03	16.74493	306.3366	−0.0003	89.58
96F2P29	0.363	0.233	0.559	3.96	24.26	19.14893	305.3387	−0.0006	89.65
96F2P30	0.438	0.233	0.857	1.71	5.64	4.713773	94.79252	−0.0012	89.63
96F2P31	0.397	0.233	0.74	1.4	7.94	7.139789	93.79687	0.0025	89.63
96F2P32	0.354	0.215	0.658	1.73	10.11	9.530105	93.79903	−0.0007	89.62
96F2P34	0.33	0.193	0.596	2.16	14.01	11.94212	110.7627	−0.0018	89.62
96F2P35	0.302	0.178	0.523	2.26	16.07	14.33964	109.7674	0.0001	89.63
96F2P36	0.275	0.16	0.472	2.47	17.21	16.81704	108.772	0.0004	89.65
96F2P37	0.256	0.169	0.452	2.47	17.04	19.16716	104.7828	−0.0007	89.65
96F2P39	0.227	0.157	0.388	2.73	17.56	23.97432	98.79517	−0.0014	89.67
96F2P40	0.443	0.274	0.845	1.7	6.78	5.928496	88.81177	−0.0003	89.69
96F2P42	0.382	0.235	0.708	6.09	10.35	8.338904	89.80965	−0.0007	89.73
96F2P43	0.309	0.172	0.556	1.98	10.95	12.00222	86.82	0.0004	89.74
96F2P44	0.269	0.166	0.47	2.22	13.67	15.61131	76.84423	0.0004	89.75
96F2P45	0.25	0.175	0.447	2.3	14	18.03457	75.84625	0.0005	89.73
96F2P46	0.239	0.156	0.394	2.41	17.07	20.4417	73.852	−0.0007	89.71
96F2P47	0.228	0.163	0.384	2.38	15.52	22.85645	73.8537	−0.0022	89.74
96F2P48	0.222	0.168	0.377	2.78	14.06	25.27281	70.86127	0.0001	89.82
96F2P50	0.407	0.225	0.754	1.06	5.98	5.976656	59.8731	0.0011	89.73
96F2P51	0.317	0.198	0.619	1.38	6.15	8.338421	58.87793	0.0002	89.80
96F2P52	0.307	0.181	0.553	1.75	9.53	10.75038	55.88542	−0.0013	89.82

Table 2
1-g Data, film thickness data

Code	δ (mm)	h (mm)	H (mm)	V_{wave} (m/s)	W_{wave} (Hz)	G_g (kg/m^2 s)	G_l (kg/m^2 s)	Pabs (kPa)
96G3P2	0.48	0.282	0.863	−0.6	11.5	5.944064	41.89765	98.37
96G3P3	0.444	0.281	0.807	−0.77	11.34	8.33607	42.89521	98.35
96G3P4	0.394	0.261	0.624	−0.14	12	10.72566	42.8962	98.62
96G3P5	0.325	0.202	0.55	1.9	17.52	13.08567	57.86132	99.33
96G3P6	0.285	0.187	0.463	1.86	16.89	15.46164	49.8816	99.57
96G3P7	0.253	0.167	0.447	2.23	14.11	17.88484	52.8745	100.50
96G3P8	0.245	0.151	0.381	2.17	20.49	20.2908	50.88041	101.15
96G3P10	0.22	0.174	0.348	2.64	13.4	25.13875	46.89195	102.97
96G3P12	0.517	0.316	0.907	−1.92	12	5.934477	80.8026	99.26
96G3P13	0.483	0.298	0.857	−0.28	12.37	8.340864	81.80017	99.68
96G3P14	0.412	0.269	0.716	1.56	14.01	10.74844	81.80205	99.86
96G3P15	0.339	0.198	0.571	2.17	13.79	13.11607	79.80688	100.33
96G3P16	0.312	0.208	0.537	2.47	16.14	15.52005	78.81111	101.26
96G3P17	0.282	0.191	0.487	2.28	14.62	17.91843	77.8153	101.95
96G3P19	0.252	0.183	0.413	2.58	18.29	22.76799	72.83049	104.19
96G3P20	0.246	0.164	0.371	2.7	20.33	25.11357	70.83514	105.20
96G3P22	0.529	0.314	0.957	2.38	13.19	4.736892	102.7466	99.77
96G3P23	0.507	0.293	0.868	0.91	13.88	7.138882	102.7466	99.68
96G3P24	0.442	0.287	0.792	1.7	10.84	9.510502	101.7514	100.66
96G3P25	0.383	0.247	0.646	1.94	18.82	11.86776	101.7514	101.17
96G3P26	0.351	0.225	0.607	2.12	16.71	14.29689	99.7586	101.67
96G3P27	0.317	0.208	0.54	2.47	19.54	16.73364	99.7609	102.94
96G3P28	0.294	0.192	0.483	2.23	19.21	19.10805	98.76329	103.77
96G3P29	0.273	0.175	0.433	2.62	20.8	21.56281	96.7703	105.43
96G3P30	0.261	0.185	0.408	2.7	21.62	23.92842	95.77267	106.92
96G3P32	0.6	0.359	1.077	2.28	10.65	4.73809	149.631	101.02
96G3P33	0.512	0.33	0.906	2.38	12.12	7.149664	150.6285	101.21
96G3P34	0.493	0.318	0.797	2.12	16.4	9.514098	150.632	102.66
96G3P35	0.412	0.267	0.681	2.62	19.22	11.90011	150.632	103.23
96G3P36	0.374	0.248	0.626	2.7	20.74	14.31369	149.6345	104.39
96G3P37	0.348	0.236	0.562	2.83	22.6	16.69089	148.6403	106.04
96G3P38	0.325	0.213	0.528	2.97	23.51	19.12844	147.6461	107.52
96G3P39	0.303	0.193	0.477	3.18	24.64	21.51485	145.6509	109.59
96G3P40	0.288	0.201	0.459	3.3	24.33	23.86244	143.659	111.96
96G3P42	0.403	0.244	0.633	2.78	23.38	14.31369	197.5175	106.83
96G3P43	0.371	0.26	0.608	3.18	20.21	16.74045	196.5199	109.52
96G3P44	0.342	0.239	0.551	3.43	22.71	19.04054	194.5293	111.53
96G3P46	0.632	0.297	1.225	3.21	9.21	3.547278	201.5031	102.04
96G3P47	0.583	0.328	0.984	2.47	13.88	5.928902	201.5031	102.88
96G3P48	0.513	0.334	0.845	2.58	17.44	8.323704	201.5031	103.92
96G3P49	0.447	0.283	0.731	3.3	20.53	10.65977	199.5126	105.63
96G3P52	0.683	0.233	1.813	2.78	5.75	2.339329	305.2332	103.14
96G3P53	0.653	0.371	1.13	3.18	14.94	4.748095	303.2382	105.64
96G3P54	0.567	0.354	0.911	3.13	18.44	7.123325	302.2477	107.19
96G3P55	0.53	0.33	0.836	3.56	21.16	9.496968	303.2452	109.43
96G3P56	0.481	0.313	0.774	3.3	21.37	11.91253	303.2452	111.09
96G3P57	0.425	0.274	0.66	3.71	25.96	14.23348	303.2452	113.89
96G3P58	0.394	0.254	0.616	4.24	24.53	16.67616	303.2522	118.30

1-g (G), the number of the flight (or ground run) in which the data was collected (2 in this case), and the parabola number (P20). In all of the data, the flow regime is annular with the following exceptions: P5, P15-P27, P32, P40-P42, P50, and P51 where the flow was transitional.

References

Azzopardi, B.J., 1986. Disturbance wave frequencies, velocities and spacing in vertical annular two-phase flow. Nuclear Engineering and Design 92, 121–133.

Bousman, W.S., 1995. Studies of Two-Phase Gas–Liquid Flow in Microgravity. NASA Contractor Report 195434.

de Jong, P., 1999. An Investigation of Film Structure and Pressure Drop in Microgravity Annular Flow. M.Sc. Thesis, University of Saskatchewan, Canada.

Lowe, D.C., 1997. A Study on Flow Regime Identification in Microgravity Gas–Liquid Flows Using a Capacitance Sensor. M.Sc. Thesis, University of Saskatchewan, Canada.

Lowe, D., Rezkallah, K.S., 1998. The Identification of Microgravity Two-Phase Flow Regimes Using Void Fraction Signals. Proceedings of the 11th International Heat Transfer Conference, Korea.

Rite, R., Rezkallah, K.S., 1994. Heat transfer in two-phase flow through a circular tube at reduced gravity, AIAA J. Thermophysics and Heat Transfer 8, 702–708.

Willetts, I.P., 1987. Non-Aqueous Annular Two-Phase Flow. Ph.D. Thesis, University of Oxford, UK.

Zhao, L., Rezkallah, K.S., 1995. Pressure drop in gas–liquid flow at microgravity conditions. Int. J. Multiphase Flow 21, 837–849.